Check for updates

RESEARCH ARTICLE

ADVANCED FUNCTIONAL MATERIALS
www.afm-journal.de

Unveiling the Curvature-Dependent Electrocatalytic Kinetics for Sulfur Redox Reaction in Li-S Chemistry

*Kao Wang, Yang Wang, Jun Wang, Hong Wang, Chenzhi Ding, Zhaobo Zheng, Yue Liu, Zhengtang Luo, and Yao Ding**

Lithium-sulfur (Li-S) batteries have suffered from serious "shuttle effect" and sluggish kinetic of sulfur redox reaction (SRR). Herein, we focus on the circumferential strain engineering on tailoring the single-atom catalysts (SACs) for fast SRR in Li-S batteries. A distinguish coaxial V-doped MoS_2@CNTs (V-MoS_2@CNTs) heterostructure with uniform biaxial strain is developed as the platform to unveil the curvature-dependent electrocatalytic kinetics in SRR. Both experimental results and theoretical calculations show that this circumferential strain not only benefits the interaction between cathodes and LiPSs, but also dynamically strengthens the SRR by a modified d-band structure of dual-metal active sites, i.e., V and Mo. Consequently, the V-MoS_2@CNTs catalysts with strong circumferential strain exhibit a discharge capacity of 1202 mAh cm^{-2} at 0.5 C and a capacity fading of 0.052% at 1 C, while an outstanding rate performance of 796 mAh g^{-1} at 5 C. In addition, a high area capacity of 3.2 mAh cm^{-2} is maintained after 65 cycles at 0.1 C with a high sulfur loading of 3.7 mg cm^{-2}. The strategy developed in this work deepens understanding the impact of curving strain engineering in SRR, and provides a feasible way to the scale-up synthesis of high-performance SACs with tunable electrocatalytic activities.

1. Introduction

Lithium-sulfur (Li-S) batteries, which have been considered as one of the most promising alternatives to lithium-ion batteries, have aroused great interest in recent years due to their intrinsic high theoretical specific capacity (1675 mAh g^{-1}) and considerable energy density (2600 Wh kg^{-1}).[1] Nevertheless, there are a number of issues that prevent the commercialization of Li-S batteries. First, sulfur and its final discharge product Li_2S have poor electrical conductivity, resulting in sluggish oxidation/reduction kinetics during charge/discharge. Second, sulfur produces a huge volume expansion of ≈80% during cycling, leading to the destruction of active materials. Third, lithium polysulfide (LiPSs) generated during the discharge process can dissolve into the electrolyte, resulting in the "shuttle effect" and leading to poor cycling stability and low coulombic efficiency.[2] Therefore, the development of electrocatalysts, which can accelerate the redox reaction of LiPSs during cycling with adsorption capacity and catalytic activity, is crucial to the scaling up of high-performance Li-S batteries with improved the reaction kinetics.[3]

In recent years, tremendous efforts have been devoted to designing electrocatalysts that can solve these drawbacks in Li-S batteries. An ideal catalyst should provide fast electron transfer, considerable adsorption area, and high catalytic activity for LiPSs during charge/discharge cycles. Taking advantage of the large surface area in layered structure, 2D transition-metal dichalcogenides (2D TMDs) have demonstrated outstanding performance as cathode hosts in Li-S batteries, e.g. MoS_2, VS_2, CoS_2, NiS_2, etc.[4] They can anchor the LiPSs through the dipole interaction between metal-S and S-Li bonds.[5] Presentively, MoS_2 has been widely reported as a promising catalyst in cathodes for Li-S batteries, owing to its intrinsic high catalytic properties and low cost.[6] Common strategies, such as defect-engineering,[7] phase engineering,[8] and structural design,[9] have been investigated for promoting the catalytic activity in sulfur redox reaction (SRR). However, the incomplete utilization of its active surface area still hinders the industrial application of MoS_2 cathodes.

Designing catalysts with single-atom catalysts (SACs) is an effective way to boost the electrocatalytic activity of redox reactions in Li-S batteries.[10] SACs with close to 100% atom utilization have superior electrochemical activity for Li-S battery cathodes.[11,8] However, less work has been reported on boosting the catalytic effects of both host materials and the doped single atoms (e.g., V, Cr, Mn). Also, the effective regulation of the

---

K. Wang, H. Wang, C. Ding, Z. Zheng, Y. Liu, Y. Ding
School of Materials Science and Engineering
Wuhan University of Technology
Wuhan 430070, P. R. China
E-mail: ydingaf@whut.edu.cn

Y. Wang
School of Optoelectronic Engineering
Chongqing University of Posts and Telecommunications
Chongqing 401331, P. R. China

J. Wang, Z. Luo
Department of Chemical and Biological Engineering and William Mong Institute of Nano Science and Technology
Hong Kong University of Science and Technology
Clear Water Bay, Kowloon, Hong Kong 999077, P. R. China

Y. Ding
Hubei Longzhong Laboratory
Xiangyang 441000, P. R. China

The ORCID identification number(s) for the author(s) of this article can be found under https://doi.org/10.1002/adfm.202422689

DOI: 10.1002/adfm.202422689

© 2025 Wiley-VCH GmbH

coordination environment of these single atoms, regarded as active sites, is the key to boost the electrocatalytic activity.

Local strain engineering, which is an effective method to uniformly control the electronic structure of TMDs in nanoscale, has been widely studied in the field of electrocatalysis.[12] For instance, Zhang et al. introduced tensile stress in MoS_2 lattice through different cooling rates.[13] Cabot et al. obtained surface strain enhanced MoS_2 by cladding on cubic Co_9S_8 surface.[14] However, the previously reported strain engineering always remain limitations, i.e., lack of dimensional control and with poor homogeneity. In addition, the ambiguous correlation between the bending strain of SACs and its electrocatalytic properties in Li-S batteries still needs to be pointed out.

Inspired by the pioneering researches, this work designs a vanadium-doped few MoS_2 (less than four layers) on carbon nanotubes (V-MoS_2@CNTs) with uniform circumferential strain as multifunctional cathode for high-performance Li-S batteries. By tailoring the V-MoS_2@CNTs heterostructures with different diameters, e.g. $\phi \approx 2$ nm, $\phi \approx 15$ nm, $\phi \approx 50$ nm, a uniform and tunable circumferential strain can be well applied in V-MoS_2 through the concentric-tube structure. Scanning transmission electron microscopy (STEM), Raman, X-ray absorption spectroscopy (XAS) characterizations confirm the changes in chemical environment of V-MoS_2@CNTs with this tunable circumferential strain. More importantly, the curvature-dependent electrocatalytic kinetics in redox reactions of LiPSs and further electrochemical performance in Li-S batteries has been detailly investigated by a series of in situ characterizations (e.g., in situ Raman and in situ XRD). Density functional theory (DFT) calculations are carried out to investigate the remarkably enhanced adsorption capability of LiPSs upon introduction of circumferential strain. The catalysts developed in this work enable the Li-S batteries to exhibit a high capacity of 1202 mAh cm^{-2} at 0.5 C and a low average capacity fading of 0.052% at 1 C, while demonstrating excellent rate performance of 796 mAh g^{-1} at a high rate of 5 C. In addition, a high area capacity of 3.2 mAh cm^{-2} is also maintained with a high sulfur loading of 3.7 mg cm^{-2}. The underlying curvature-dependent electrocatalytic mechanism revealed in this work can provide guidance to optimize rate-determining step (RDS) in redox reactions of LiPSs, and showing great potential for practical applications in electrocatalytic energy storage devices beyond Li-S batteries, e.g. metal-air batteries and redox flow batteries.

2. Results and Discussion

Figure 1a presents the schematic synthesis of coaxial vanadium-doped MoS_2@CNTs (V-MoS_2@CNTs) heterostructures with uniform circumferential strain in V-doped MoS_2 layers. Importantly, acid treatment should be conducted on CNTs with different diameters to improve the hydrophilicity before synthesis. After this, coaxial MoS_2 and CNTs heterostructures (MoS_2@CNTs) are obtained by annealing CNTs at 700 °C using molybdenum source and sulfur powder.[15] V-MoS_2@CNTs are obtained by annealing MoS_2@CNTs with additional vanadium source (Experimental Methods in Supporting Information for details). Three types of CNTs with different diameters are used for investigating the effect of this uniform circumferential strain on the electrocatalytic behavior in Li-S batteries. Namely, V-MoS_2@CNT_1 (V-doped MoS_2 on single-wall CNTs with $\phi_{CNT} = \sim 2$ nm), V-MoS_2@CNT_2 (V-doped MoS_2 on multi-wall CNTs with $\phi_{CNT} = \sim 15$ nm) and V-MoS_2@CNT_3 (V-doped MoS_2 on multi-wall CNTs with $\phi_{CNT} = \sim 50$ nm) are prepared.

In order to carefully observe the heterointerface and the local atomic structure of V-MoS_2@CNTs heterostructures, high-resolution transmission electron microscopy (HRTEM) images for V-MoS_2@CNTs are provided in Figure 1b,d. The coaxial tube-structure of V-MoS_2@CNTs can be clearly seen in Figure S26 (Supporting Information). Figure 1b shows V-MoS_2@CNT_1 of single-wall CNTs coated with 2–3 layers of 2H phase V-MoS_2 (d = 6.27 Å), referring to the crystal plane of MoS_2 (002), which maintains the same results of other V-MoS_2@CNTs samples in Figure S1 (Supporting Information), Figure 1c,d. It should be pointed out that the less layers of V-MoS_2 should result in the stronger circumferential strain in V-MoS_2 with obvious smaller curvature of the tubes, which is verified to be important for the acceleration of electrocatalytic kinetics of SRR in Li-S batteries. Besides, Figure 1e–h display the high-angle annular dark-field scanning transmission electron microscopy (HAADF-STEM) image of V-MoS_2@CNT_1, together with the corresponding energy dispersive X-ray spectroscopy (EDX) results, which demonstrates the uniformly distribution of Mo, S and V elements in the heterostructures. Notably, V dopants are successfully supported by the presence of slight vanadium signals in Figure 1h, due to the few amounts of V dopants in samples (1 wt.%, Table S1, Supporting Information). Additionally, TG (Figure S28, Supporting Information) and ICP-OES results indicate that MoS_2 in different samples are relatively with the same amount, which excludes the influence of proportional variation in the following electrochemical behavior. The HAADF-STEM image and EDX results of V-MoS_2@CNT_2 and V-MoS_2@CNT_3 are also showed in Figures S2 and S3 (Supporting Information). Figure 1i shows that V-MoS_2 (100) layers on CNT in V-MoS_2@CNT have the lattice distance $d_{(100)}$ = 2.80 Å. Compared with the standard lattice distance of MoS_2 (100), $d_{(100)}$ = 2.74 Å, the circumferential strain in V-MoS_2@CNT endows a larger lattice spacing. In addition to get a direct view of the strain distribution in V-MoS_2@CNT, Figure 1j,k plot the strain distribution of the wrapped V-MoS_2 in V-MoS_2@CNT. Here, Figure 1k is the corresponding strain distribution along ϵ_{xy} direction of V-MoS_2 in Figure 1j. It finds that a symmetric and uniform bi-direction tensile strain has been applied in V-MoS_2 among the radial direction of inside CNTs.

In order to observe the circumferential strain effects on elemental phase states and chemical environment in V-MoS_2@CNTs heterostructures, X-ray diffraction (XRD) technique is applied on MoS_2@CNTs and V-MoS_2@CNTs. Here, characteristic peaks of MoS_2 crystal faces, matched well with standard MoS_2 (JCPDS No. 75–1539), appeal on all samples, respectively. No other peaks associated to V elements are detected in XRD patterns, which suggested the atomic distribution of V atoms in V-MoS_2@CNTs. Additionally, diffraction peaks at 26°and 42° can be attributed to CNTs, of which V-MoS_2@CNT_3 occupies the highest peak intensity due to the multi-wall structures. **Figure** 2b enlarges the diffraction peak of MoS_2 (100) at ≈33° in V-MoS_2@CNTs, in which a slight shift of the peak position to small angle is observed with the decreases of diameters, due to the increasing interplanar spacing of MoS_2 (100). In addition, for the Raman spectra in Figure 2c, two characteristic peaks

© 2025 Wiley-VCH GmbH

16163028, 2025, 26, Downloaded from https://advanced.onlinelibrary.wiley.com/doi/10.1002/adfm.202422689 by WUHAN UNIVERSITY OF TECHNOLOGY, Wiley Online Library on [05/09/2025]. See the Terms and Conditions (https://onlinelibrary.wiley.com/terms-and-conditions) on Wiley Online Library for rules of use; OA articles are governed by the applicable Creative Commons License

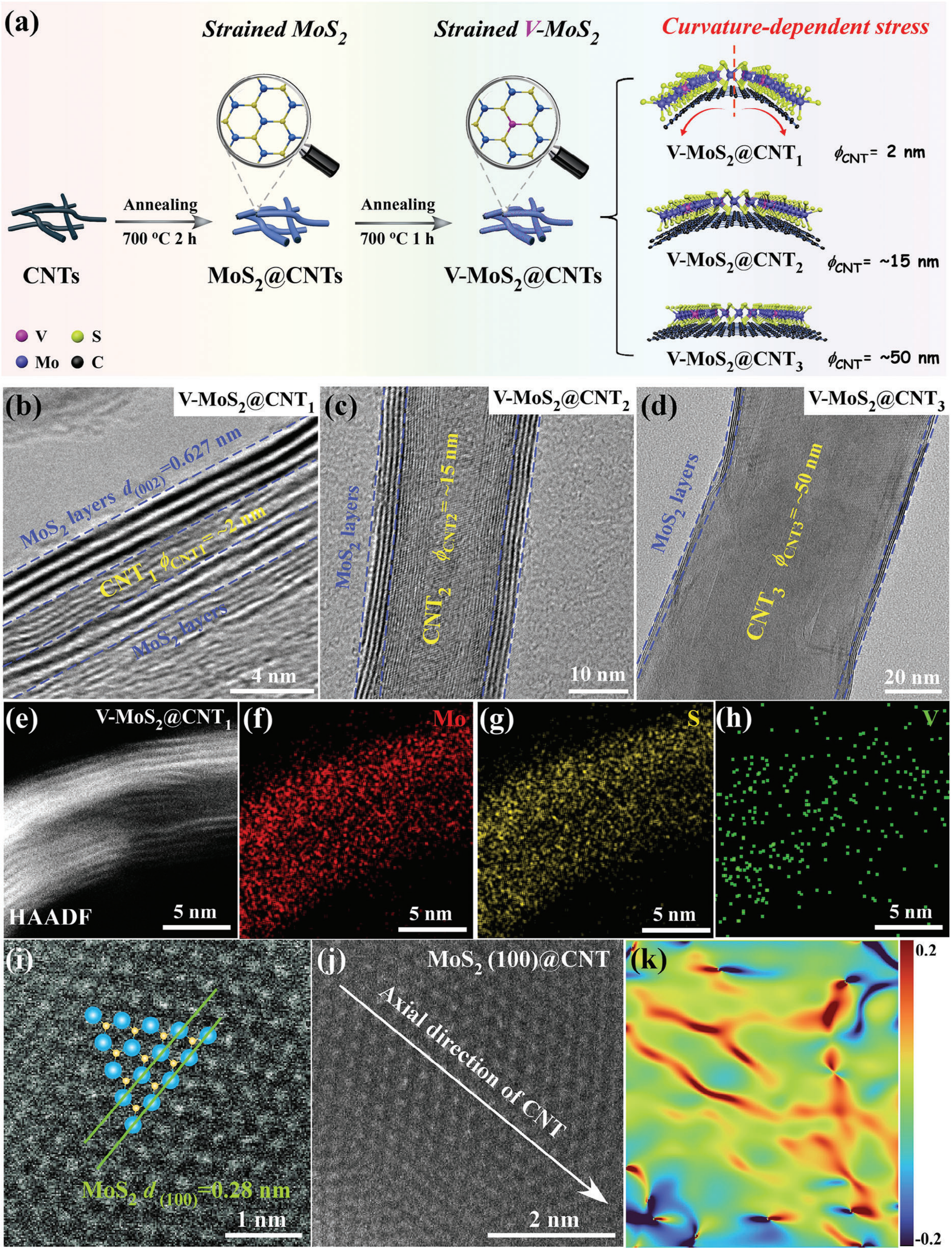

Figure 1. Coaxial V-doped MoS_2@CNTs (V-MoS_2@CNTs) heterostructures with uniform circumferential strain. a) Schematic diagram of the synthetic procedure of MoS_2/CNTs heterostructure with different diameters for CNTs (ϕ_{CNT}). b–d) HRTEM images of V-MoS_2@CNT_1 (b), V-MoS_2@CNT_2 (c), and V-MoS_2@CNT_3 (d), respectively. e–h) HAADF-STEM (e) and elemental mapping images of Mo (f), S (g), and V (h) in V-MoS_2@CNT_1. i,j) STEM image of the MoS_2 (100) on CNT and the corresponding strain distribution of (j) in (k).

16163028, 2025, 26, Downloaded from https://advanced.onlinelibrary.wiley.com/doi/10.1002/adfm.202422689 by WUHAN UNIVERSITY OF TECHNOLOGY, Wiley Online Library on [05/09/2025]. See the Terms and Conditions (https://onlinelibrary.wiley.com/terms-and-conditions) on Wiley Online Library for rules of use; OA articles are governed by the applicable Creative Commons License

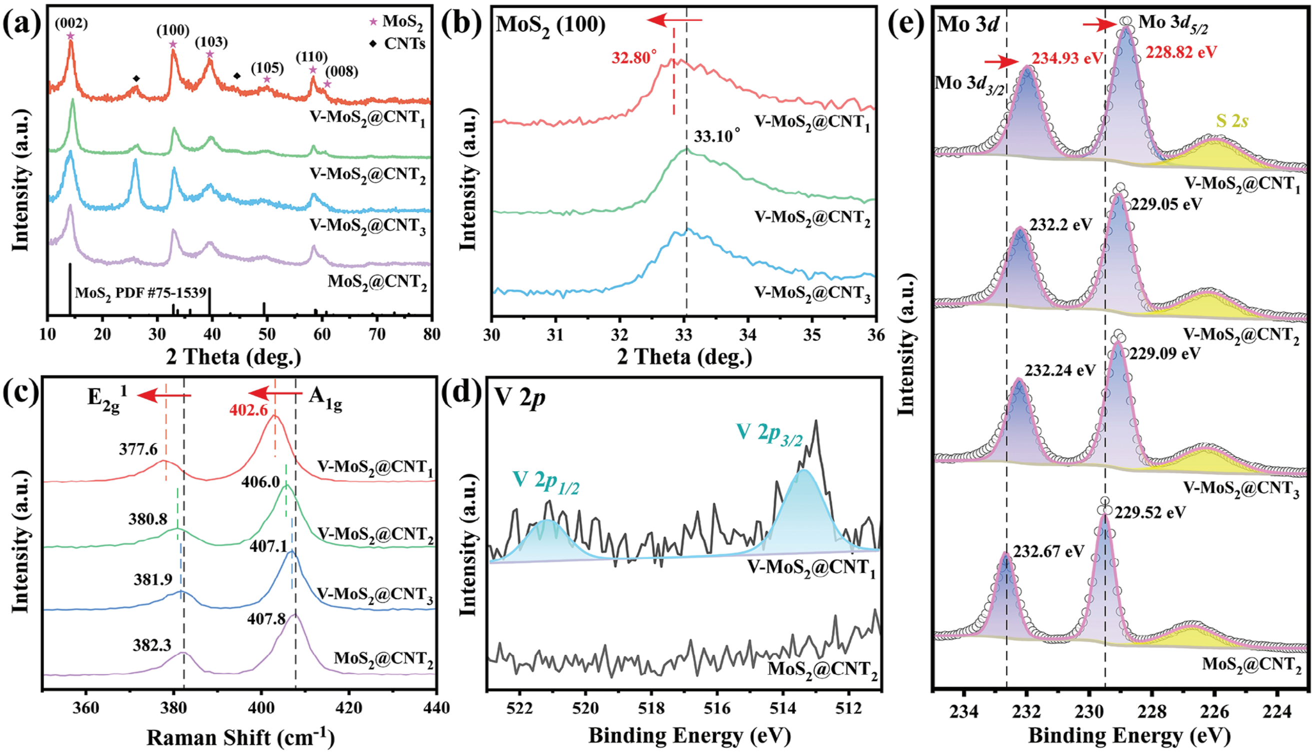

Figure 2. Characterizations of V-MoS_2@CNTs heterostructures. a) XRD patterns of MoS_2@CNT_2 and V-MoS_2@CNTs with different diameters. b) magnified regions of (a) to show the shift of characteristic peak of MoS_2 (100). c) Raman spectra of $E_{2g}{}^1$ and $A_{1\ g}$ modes in MoS_2@CNT_2 and V-MoS_2@CNTs heterostructures. d) XPS spectra of V *2p* peaks of MoS_2@CNT_2 and V-MoS_2@CNTs. e) XPS spectra of Mo *3d* peaks of MoS_2@CNT_2 and V-MoS_2@CNTs heterostructures.

at 378 cm^{-1} and 403 cm^{-1} are assigned to $E_{2g}{}^1$ and $A_{1\ g}$ modes of MoS_2, respectively.[16] By comparing the peak positions of V-MoS_2@CNT_1, V-MoS_2@CNT_2, and V-MoS_2@CNT_3, a slight red-shift can be observed, indicating the successful introduction of strain.[13] V-MoS_2@CNT_1 occupies the largest shift, which should correspond to the highest strain effect. Moreover, by comparing peak positions in V-MoS_2@CNT_2 and MoS_2@CNT_2 (CNTs with same diameters), it shows that both peaks also have a red-shift, suggesting that V doping effect leads to a change in the vibration of in-plane and out-of-plane S-Mo-S bonds.[16]

Additionally, the elemental states of V-MoS_2@CNTs heterostructures with different diameters are analyzed by X-ray photoelectron spectroscopy (XPS) in Figure 2d,e (total spectra in Figure S3, Supporting Information). As shown in Figure 2d, dual peaks, at ≈513.5 and 520.7 eV respectively attributed to V $2p_{3/2}$ and V $2p_{1/2}$ orbitals, are observed in V-MoS_2@CNT_1, whereas no associated peaks can be detected in MoS_2@CNT_2. At the meantime, characteristic peaks that belong to V dopants also presented in V-MoS_2@CNT_2 and V-MoS_2@CNT_3 as shown in Figure S4 (Supporting Information). The abovementioned evidences indicate the successful doping of V atoms in heterostructures as the oxidation states of V^{4+}, which is also consistent with the TEM-EDX mapping results. Besides, the core-level of Mo XPS spectra for MoS_2@CNT and V-MoS_2@CNT heterostructures are presented in Figure 2e, in which the binding energy locating at 228.82, 234.93, and 226 eV are corresponded to the Mo $3d_{3/2}$, Mo $3d_{5/2}$, and S *2s* orbitals in V-MoS_2@CNT_1, respectively. The predominant valence state of Mo species is determined to be +4, which is consistent with the formation of MoS_2 layers. Here, compared with pure MoS_2@CNT_2, V-doped heterostructures behave a lower binding energy in dual peaks of Mo *3d*, indicating that the nearby V dopants can change the electronic structure of MoS_2 by lowering its Fermi level.[17] Besides, when compared with the signals of Mo *3d* in V-MoS_2@CNT_1, it can be found that dual peaks of Mo *3d* shift to higher binding energy in V-MoS_2@CNT_2 and V-MoS_2@CNT_3, indicating that circumferential strain can increase the electronic aggregation on V-MoS_2 surface.[18] It should be pointed out that the aforementioned characterizations clearly indicate that no MoO_2 or other Mo-derived crystal phases are formed by this strategy instead of MoS_2. Besides, the high-resolution S *2p* spectra of different samples in Figure S27 (Supporting Information) have shown that no S_8 remains in the original materials.

To further explore coordination information of V atoms and curvature-dependent bonding environment in V-MoS_2@CNTs heterostructures, X-ray absorption fine structure (XAFS) analyses are carried out. As shown in **Figure** 3a, X-ray near-edge absorption fine structure (XANES) spectra of V K-edge present that the absorption edges of V-MoS_2@CNT_1, V-MoS_2@CNT_2, and V-MoS_2@CNT_3 are located between V foils and VO_2, which indicates the partially oxidated V states in heterostructures.[19] Besides, white-line peaks intensity of V-MoS_2@CNT heterostructures exhibit a trend of V-MoS_2@CNT_1 > V-MoS_2@CNT_2 > V-MoS_2@CNT_3. Here, the intensity of white-line peaks should

© 2025 Wiley-VCH GmbH

16163028, 2025, 26, Downloaded from https://onlinelibrary.wiley.com/doi/10.1002/adfm.202422689 by WUHAN UNIVERSITY OF TECHNOLOGY, Wiley Online Library on [05/09/2025]. See the Terms and Conditions (https://onlinelibrary.wiley.com/terms-and-conditions) on Wiley Online Library for rules of use; OA articles are governed by the applicable Creative Commons License

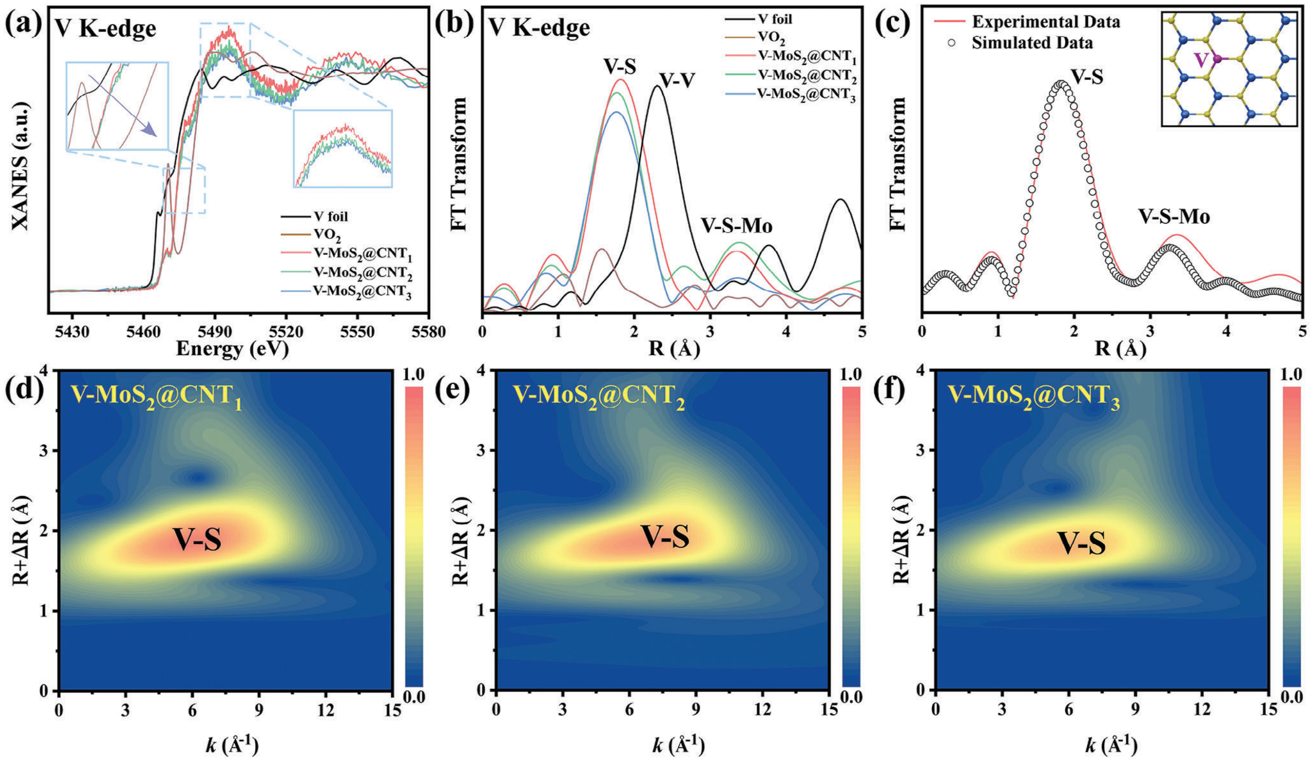

Figure 3. XANES characterizations of V-MoS$_2$@CNTs heterostructures. a) V K-edge XANES spectra for V-MoS$_2$@CNTs heterostructures, VO$_2$, and V foil. b) FT-EXAFS spectra of V K-edge in V-MoS$_2$@CNTs heterostructures, VO$_2$, and V foil in k^2 weighted R-space. c) EXAFS fitting curves of V K-edge in V-MoS$_2$@CNT$_1$ (inset: atomic V-doping in MoS$_2$@CNT$_1$). d–f) The wavelet transforms (WT) images of V-MoS$_2$@CNT$_1$ (d), V-MoS$_2$@CNT$_2$, (e) and V-MoS$_2$@CNT$_3$ (f) at V K-edge.

relate to the transfer of inner electrons in V atoms from 1*s*- to the 4*p*-orbitals, which implies that the strengthened V-S bonds can facilitate the electrons transfer,[20] i.e., V-MoS$_2$@CNT$_1$ heterostructures occupy more electrons in V 4*p*-orbitals.

In addition, Fourier transform extended X-ray absorption fine structure (FT-EXAFS) spectra of V-MoS$_2$@CNTs heterostructures, VO$_2$, and V foil are also plotted in Figure 3b. Specifically, compared with the spectra of VO$_2$ and V foil, V-MoS$_2$@CNTs heterostructures with different diameters show distinctive peaks at ~1.81 Å, which is represented for V-S coordination, as well as peaks at ~3.2 Å correspond to the second-shell V-S-Mo coordination.[21] It is worth noting that R-space peaks in EXAFS spectra should correspond to the spatial position of atoms instead of direct bonding information. Thus, no direct V-V bonding signal is detected, which proves the single-atomic V dopants in V-MoS$_2$@CNTs heterostructures rather than V clusters. Moreover, Figure 3c gives EXAFS fitting results of V-MoS$_2$@CNT$_1$, together with the structural parameters in Table S2 (Supporting Information), which indicates that the average coordination numbers of V-S (CN$_{\text{V-S}}$) equal to 5.84 for V-MoS$_2$@CNT$_1$. Compared with that for V-MoS$_2$@CNT$_2$ (CN$_{\text{V-S}}$ = 5.77) and V-MoS$_2$@CNT$_3$ (CN$_{\text{V-S}}$ = 5.61) in Figure S5 (Supporting Information), V-MoS$_2$@CNT$_1$ possess the highest CN$_{\text{V-S}}$ value due to the strongest circumferential stress. Figure 3d–f depict the wavelet transform images of EXAFS (WT-EXAFS) for V-MoS$_2$@CNT heterostructures with different diameters and V foil (κ = 10, and σ = 1). All three samples show distinct V-S resolved spectra, in which V-MoS$_2$@CNT$_1$ has the V-S signal in k-space of 6.05 A^{-1}, V-MoS$_2$@CNT$_2$ has that of 6.20 A^{-1} and V-MoS$_2$@CNT$_3$ has that of 6.35 A^{-1}, respectively, as well as the highest intensity of V-S bonds. These also evident that V-MoS$_2$@CNT$_1$ has the most strengthened V-S bonds and strongest elemental interaction due to the circumferential strain caused by inside SWCNTs.

Important capabilities of electrodes, i.e., the adsorption and conversion of soluble LiPSs, are crucial for the capacity and performance of Li-S batteries. To elucidate the curvature-dependent electrocatalytic properties in Li-S chemistry, standard Li$_2$S$_6$ adsorption experiment is conducted on V-MoS$_2$@CNTs heterostructures and MoS$_2$@CNT$_2$ with Li$_2$S$_6$ solution (5 mL, 2 mmol L^{-1}). Visualized adsorption results are performed in the inset of **Figure 4a**, together with the ultraviolet-visible (UV-vis) spectra acquired from the supernatant of solutions after adsorption. After 6 h adsorption, Li$_2$S$_6$ electrolyte with V-MoS$_2$@CNT$_1$ catalysts become completely decolorized, whereas samples with other catalysts show incompletely fading. This indicates the outstanding adsorption performance of V-MoS$_2$@CNT$_1$ and the crucial role of circumferential strain in LiPSs adsorption. Besides, characteristic peaks of S$_6{}^{2-}$ in UV–vis spectra also disappear in the supernatant of solutions with V-MoS$_2$@CNT$_1$ catalysts,[22] which is consistent with the result of abovementioned visualized Li$_2$S$_6$ adsorption test.

Furthermore, electrochemical test conducted on the symmetric cell with 0.25 M Li$_2$S$_6$ provide deeper insight into the curvature-dependent LiPSs conversion properties of

© 2025 Wiley-VCH GmbH

16163028, 2025, 26, Downloaded from https://advanced.onlinelibrary.wiley.com/doi/10.1002/adfm.202422689 by WUHAN UNIVERSITY OF TECHNOLOGY, Wiley Online Library on [05/09/2025]. See the Terms and Conditions (https://onlinelibrary.wiley.com/terms-and-conditions) on Wiley Online Library for rules of use; OA articles are governed by the applicable Creative Commons License

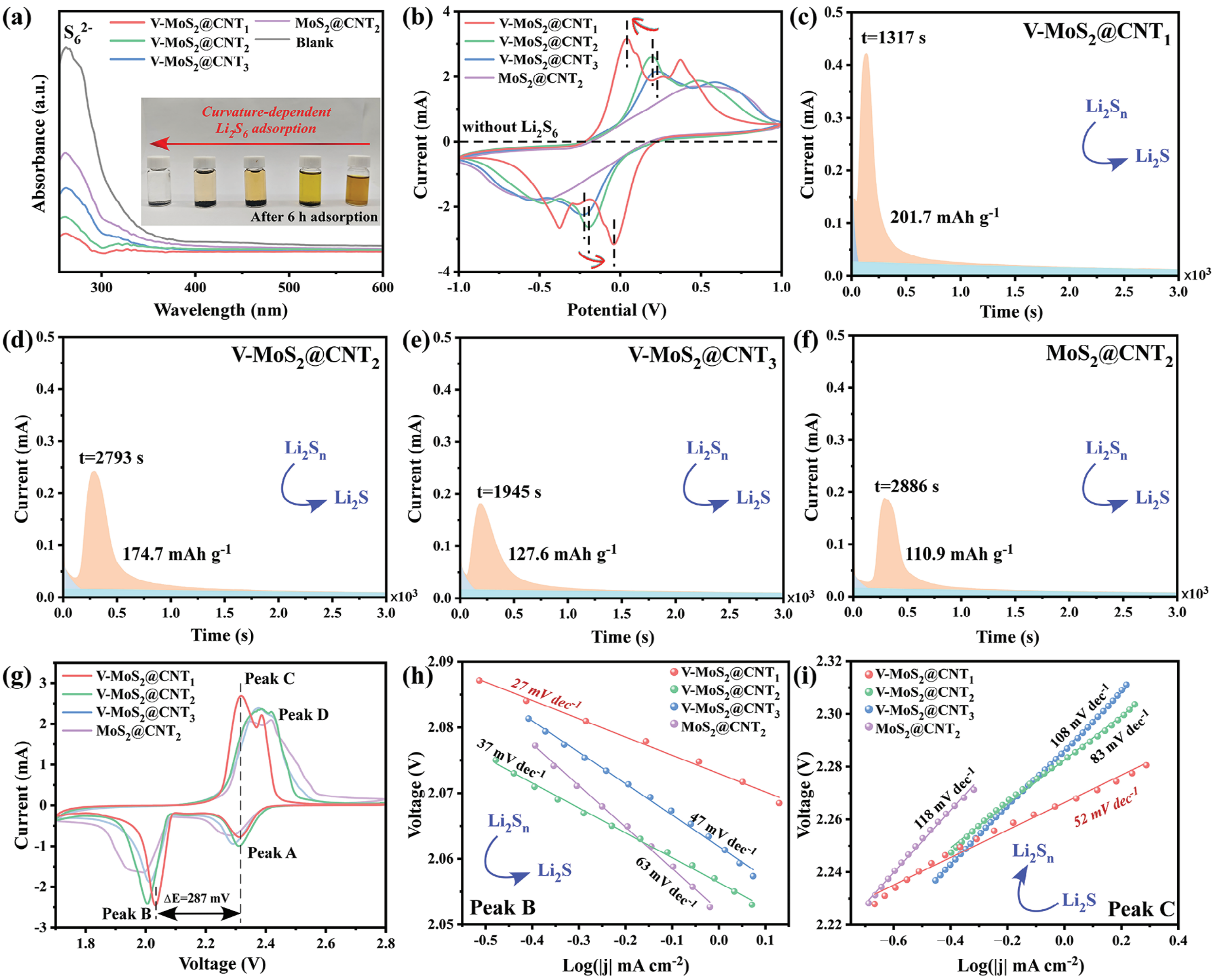

Figure 4. LiPSs adsorption and conversion kinetics for V-MoS$_2$@CNTs heterostructures. a) UV–vis spectra and digital photo (inset) of standard Li_2S_6 adsorption test for V-MoS$_2$@CNTs heterostructures with different diameters. b) CV cures of Li_2S_6 symmetric cells with V-MoS$_2$@CNT$_1$, V-MoS$_2$@CNT$_2$, V-MoS$_2$@CNT$_3$, and MoS$_2$@CNT electrodes at 2 mV s^{-1}. c–f) Potentiostatic nucleation test of Li_2S on V-MoS$_2$@CNT$_1$ (c), V-MoS$_2$@CNT$_2$ (d), V-MoS$_2$@CNT$_3$ (e), and MoS$_2$@CNT (f) electrodes discharged at 2.05 V. g) CV curves of V-MoS$_2$@CNT$_1$/S, V-MoS$_2$@CNT$_2$/S, V-MoS$_2$@CNT$_3$/S, and MoS$_2$@CNT$_2$/S electrodes at 0.1 mV s^{-1}. h,i) Corresponding Tafel plots of Peak B (h) and Peak C (i) in (g) for different electrodes.

V-MoS$_2$@CNTs heterostructures. As shown in Figure 4b, cyclic voltammograms (CV) test conducted on V-MoS$_2$@CNTs with different diameters at a scan rate of 2 mV s^{-1} confirm the superior catalytic performance of V-MoS$_2$@CNT$_1$ on the LiPSs conversion. Specifically, compared with V-MoS$_2$@CNT$_2$ and V-MoS$_2$@CNT$_3$, V-MoS$_2$@CNT$_1$ catalysts demonstrate the higher current density, sharper redox peaks, and lower redox potential, which indicates a faster LiPSs conversion kinetics.[23] For V-MoS$_2$@CNT$_1$ catalysts, they show two pairs of distinct redox peaks at 0.043/-0.039 V and 0.375/-0.376 V, in which the anodic peaks at 0.043 and 0.375 V should refer to the oxidation of Li_2S/Li_2S_2 to long-chain LiPSs and further conversed to S_8. Meanwhile, the corresponding cathodic peaks at -0.039 and -0.376 V refer to the opposite reduction steps. Notably, distinctive redox peaks appeared at -0.261/0.266 V and 0.1/-0.102 V are observed in V-MoS$_2$@CNT$_1$ catalysts, which should be attributed to the conversion between long-chain polysulfides.[24] Nevertheless, V-MoS$_2$@CNT$_2$, V-MoS$_2$@CNT$_3$, and MoS$_2$@CNT catalysts have no obvious redox peaks at this potential, which further confirms the sluggish conversion kinetics in catalysts beyond V-MoS$_2$@CNT$_1$.

In addition, Li_2S precipitation kinetic experiments are conducted on V-MoS$_2$@CNTs heterostructures with different diameters and MoS$_2$@CNT electrodes to explore their liquid-solid transition ability of LiPSs to Li_2S. As shown in Figure 4c–f, in comparison to V-MoS$_2$@CNT$_2$ (174.7 mAh g^{-1}, 2793 s), V-MoS$_2$@CNT$_3$ (127.6 mAh g^{-1}, 1945 s) and MoS$_2$@CNT (110.9 mAh g^{-1}, 2886 s) electrodes, it can be observed that V-MoS$_2$@CNT$_1$ electrodes exhibit both the highest capacity and the shortest conversion time (201.7 mAh g^{-1}, 1317 s). This indicates that circumferential strain in V-MoS$_2$@CNT heterostructures can effectively accelerate the nucleation and growth of Li_2S, as well as the V-doping

© 2025 Wiley-VCH GmbH

16163028, 2025, 26, Downloaded from https://advanced.onlinelibrary.wiley.com/doi/10.1002/adfm.202422689 by WUHAN UNIVERSITY OF TECHNOLOGY, Wiley Online Library on [05/09/2025]. See the Terms and Conditions (https://onlinelibrary.wiley.com/terms-and-conditions) on Wiley Online Library for rules of use; OA articles are governed by the applicable Creative Commons License

contribution. To further investigate the effect of circumferential strain on bi-directional sulfur redox ability of V-MoS_2@CNTs heterostructures, Li_2S dissolution experiments are also carried out by using different electrodes (Figure S6, Supporting Information). Also, V-MoS_2@CNT_1 electrodes (578.7 mAh g^{-1}, 936 s) exhibit the highest Li_2S dissolution capacity and the shortest conversion time, which far exceeds that of V-MoS_2@CNT_2 (539.7 mAh g^{-1}, 1448 s) electrodes, V-MoS_2@CNT_3 (439.6 mAh g^{-1}, 1069 s) and MoS_2@CNT (307.1 mAh g^{-1}, 1468 s). These results imply that V-MoS_2@CNT_1 electrodes with the strongest circumferential strain can effectively accelerate the bi-directional conversion between LiPSs and Li_2S, thus improving the electrochemical performance in Li-S batteries.[25]

Furthermore, to prove the underlying catalytic mechanism in the outstanding property of V-MoS_2@CNT_1 electrodes, the polarization voltage of LiPSs conversion is determined by using the CV method, which is conducted on coin cells assembled with V-MoS_2@CNT_1/S, V-MoS_2@CNT_2/S, V-MoS_2@CNT_3/S, and MoS_2@CNT/S cathodes (see Experimental Section for details, Supporting Information). Besides, TG analyses of the amount of S in each electrodes show consistent result, which infers to the limited influence of proportional variation in active materials (Figure S29, Supporting Information). CV curves of different electrodes at a scan rate of 0.1 mV/s have been presented in Figure 4g. Here, two reduction peaks appearing at 2.2–2.4 V (Peak A) and 1.9–2.1 V (Peak B) are related to the conversion of S to soluble Li_2S_x ($4 \leq x \leq 8$) and further conversion to Li_2S/Li_2S_2 during discharge. Meanwhile, two distinct oxidation peaks at 2.3–2.5 V (Peak C and Peak D) are attributed to the conversion of Li_2S/Li_2S_2 to Li_2S_x and further to S_8 during charge. It is observed that V-MoS_2@CNT_1/S electrodes show the minimum polarization voltage (ΔE) of 287 mV. In contrast, V-MoS_2@CNT_2/S, V-MoS_2@CNT_3/S and MoS_2@CNT/S electrodes exhibit larger polarization voltages and smaller current density, which suggests that V-MoS_2@CNT_1/S electrodes can effectively reduce the active energy barrier of LiPSs conversion, thereby enhancing the stability and cycling life of Li-S batteries. In addition, Tafel slopes calculated from the abovementioned CV curves elucidate the catalytic kinetics of these V-MoS_2@CNTs heterostructures with different diameters.[26] For the transition from S_8 to Li_2S_x (Figure S7, Supporting Information), the V-MoS_2@CNT_1/S electrodes has the smallest Tafel slopes. Besides, for the conversion of soluble Li_2S_x to Li_2S/Li_2S_2 (Peak B), which is always regarded as the step contributed the most to capacity, V-MoS_2@CNT_1/S electrodes show significant smaller Tafel slopes of 27 mV dec^{-1}, in comparison to that of V-MoS_2@CNT_2/S (37 mV dec^{-1}), V-MoS_2@CNT_3/S (47 mV dec^{-1}), and MoS_2@CNT/S (63 mV dec^{-1}) electrodes (Figure 4h). Meanwhile, in Figure 4i, Tafel slope of V-MoS_2@CNT_1/S electrodes for the opposite reaction (Li_2S/Li_2S_2 to Li_2S_x) is also the smallest (52 mV dec^{-1}) one among all cathodes. These electrochemical results further indicate that the circumferential strain in V-MoS_2@CNTs can accelerate the catalytic conversion reaction between S and Li_2S, further improve the thermodynamics and kinetics of reactions, which should lead to a boosted capacity and cycling stability in Li-S batteries.

To further verify the abovementioned circumferential strain effect of V-MoS_2@CNTs in the redox reaction of LiPSs, coin-type batteries are assembled with cathodes of different catalysts for electrochemical performance tests. **Figure** 5a displays the electrochemical impedance spectroscopy (EIS) spectrum of cells using V-MoS_2@CNT_1/S, V-MoS_2@CNT_2/S, V-MoS_2@CNT_3/S and MoS_2@CNT/S as electrodes. Specifically, the charge-transfer resistance (R_{ct}) value of V-MoS_2@CNT_1/S electrodes (12.9 Ω) batteries is lower than that of V-MoS_2@CNT_2/S (28.3 Ω), V-MoS_2@CNT_3/S (32.8 Ω) and MoS_2@CNT_2/S (55.4 Ω), indicating that the circumferential strain can accelerate the electron transfer.[27] The galvanostatic charge-discharge (GCD) curves at 0.2 C (1 C = 1675 mAh g^{-1}) are displayed in Figure 5b, V-MoS_2@CNT_1 cathodes have the highest discharge specific capacity of 1462.9 mAh g^{-1} compared with V-MoS_2@CNT_2 (1321.4 mAh g^{-1}), V-MoS_2@CNT_3 (1308 mAh g^{-1}) and MoS_2@CNT (1203.6 mAh g^{-1}) at 0.2 C. It exists two distinctive discharge plateaus and one charging plateau within one cycle, which is consistent with the CV curves. Here, the first discharge plateau belongs to the formation of soluble LiPSs ($S_8 \rightarrow Li_2S_8 \rightarrow Li_2S_6 \rightarrow Li_2S_4$), and the second discharge plateau corresponds to the conversion of soluble LiPSs to Li_2S_2/Li_2S ($Li_2S_4 \rightarrow Li_2S_2 \rightarrow Li_2S$). Besides, Q_1 and Q_2 are used to define the specific capacity derived from the first and second discharge platforms. The voltage difference between two platforms is defined as the polarization potential (ΔE). In addition, V-MoS_2@CNT_1 cathode has the lowest ΔE of 161 mV and highest Q_2/Q_1 ratio of 2.74 (Figure 5c), which further indicates that the circumferential strain can improve the kinetics of sulfur anodic redox reaction.[28]

In order to further investigate the circumferential strain effect on ionic transfer and conversion kinetics of Li-S chemistry, the galvanostatic intermittent titration (GITT) tests are performed (Figure 5d; Figure S8, Supporting Information) on different cathodes. The open-circuit-voltages (OCV) are obtained by holding at 0.2 C for 10 min and quasi-open-circuit-voltages (QOCV) are obtained after 30 min of resting. The transfer internal resistance of the four different cathodes is calculated according to the following Equation (1).[27]

$$\Delta R_{\text{internal}}\,(\Omega) = \left|\Delta V_{QOCV-OCV}\right| / I_{applied} \qquad (1)$$

where ΔV refers to the voltage difference between QOCV and OCV, $I_{applied}$ denotes the applied current, and $\Delta R_{internal}$ represents the internal resistance of battery during lithiation/delithiation process. The internal resistance of four heterostructures in different states has been presented in Figure 5e. Here, V-MoS_2@CNT_1 cathode exhibits the lowest internal resistance at the Li_2S nucleation and activation positions, which inhibits the excellent chemisorption and electrocatalytic ability.

Additionally, the batteries based on V-MoS_2@CNT_1/S cathode also have well rate performance. As shown in Figure 5f, V-MoS_2@CNT_1/S cathode present the specific capacities of 1275.7, 1116.9, 1035.4, 964.4, 905.7, 847.3, and 796.7 mAh g^{-1} at 0.2, 0.5, 1, 2, 3, 4, and 5 C, respectively. Then, when the current density recovered from 5 C to 0.5 C, the discharge capacity also recovers to 1112.7 mAh g^{-1}, and the resulting calculated energy density at different current densities are shown in Figure S32 (Supporting Information). Moreover, the specific capacity of V-MoS_2@CNT_1 (796.7 mAh g^{-1}) is much higher than that of other cathodes at 5 C. This demonstrates the excellent rate capability and outstanding reversibility of V-MoS_2@CNT_1

16163028, 2025, 26, Downloaded from https://advanced.onlinelibrary.wiley.com/doi/10.1002/adfm.202422689 by WUHAN UNIVERSITY OF TECHNOLOGY, Wiley Online Library on [05/09/2025]. See the Terms and Conditions (https://onlinelibrary.wiley.com/terms-and-conditions) on Wiley Online Library for rules of use; OA articles are governed by the applicable Creative Commons License

16163028, 2025, 26, Downloaded from https://onlinelibrary.wiley.com/doi/10.1002/adfm.202422689 by WUHAN UNIVERSITY OF TECHNOLOGY, Wiley Online Library on [05/09/2025]. See the Terms and Conditions (https://onlinelibrary.wiley.com/terms-and-conditions) on Wiley Online Library for rules of use; OA articles are governed by the applicable Creative Commons License

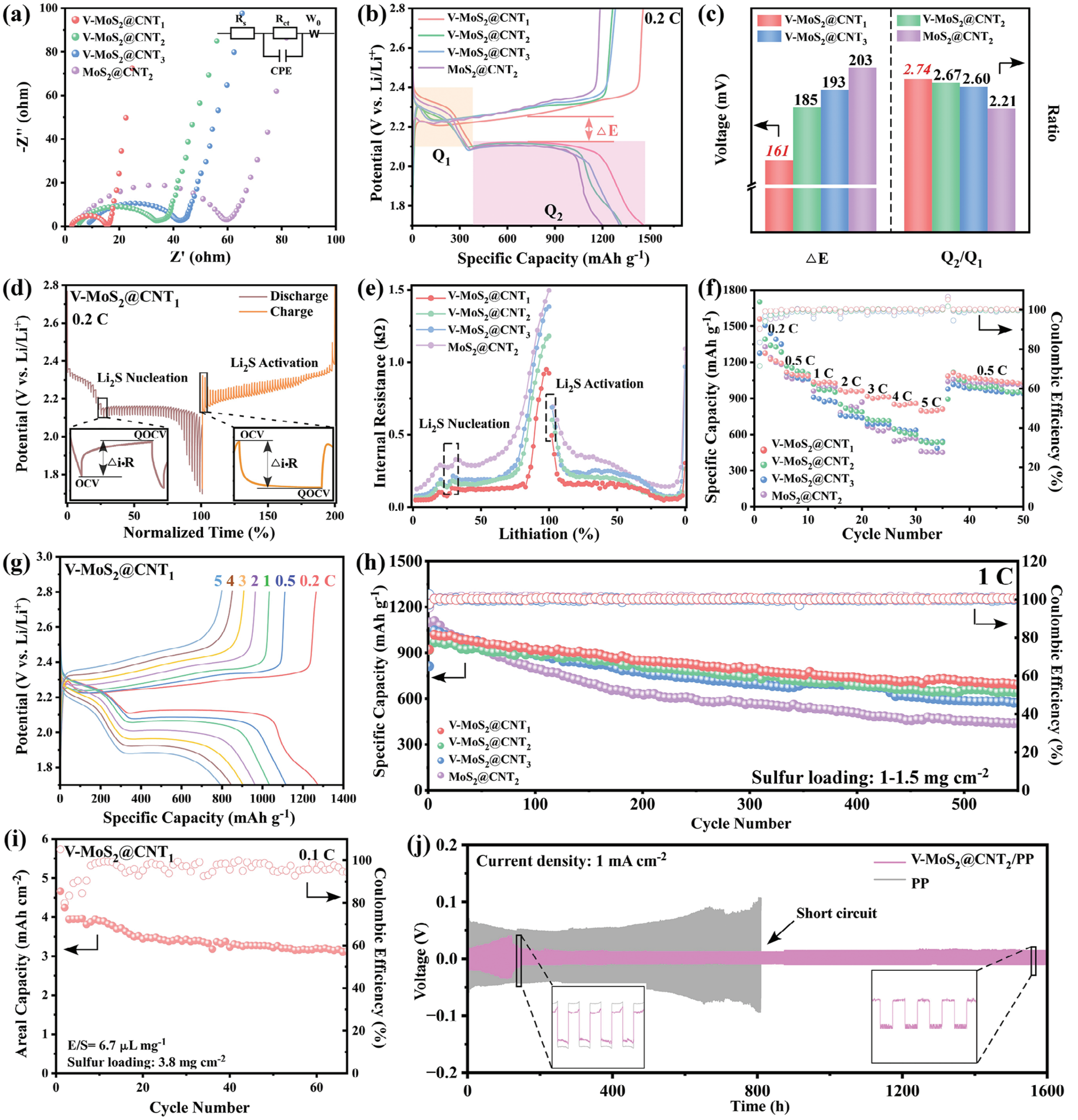

Figure 5. Electrochemical performance of Li-S batteries with V-MoS$_2$@CNTs heterostructures as cathodes. a) Nyquist plots of V-MoS$_2$@CNT$_1$/S, V-MoS$_2$@CNT$_2$/S, V-MoS$_2$@CNT$_3$/S and MoS$_2$@CNT$_2$/S cathodes. b) GCD profiles at 0.2 C for different cathodes. c) Polarization potential and Q$_2$/Q$_1$ ratios of Li-S batteries with different cathodes. d) GITT results of charge/discharge process of V-MoS$_2$@CNT$_1$/S cathodes at 0.2 C. e) The corresponding internal resistances of four cathodes. f) Rate performances of different cathodes. g) Charge/discharge profiles at different current densities with V-MoS$_2$@CNT$_1$/S cathode. h) Long cycling performances of V-MoS$_2$@CNT$_1$/S, V-MoS$_2$@CNT$_2$/S, V-MoS$_2$@CNT$_3$/S and MoS$_2$@CNT$_2$/S cathodes at 1 C. i) Cycling performances of V-MoS$_2$@CNT$_1$/S cathode with high sulfur loading. j) Voltage-time curves of Li||Li symmetric batteries with PP and V-MoS$_2$@CNT$_2$/PP separators, respectively.

cathodes. Figure 5g shows the GCD curves of V-MoS$_2$@CNT$_1$ cathodes at different current densities (from 0.2 C to 5 C). In contrast, the GCD curves of V-MoS$_2$@CNT$_2$, V-MoS$_2$@CNT$_3$ and MoS$_2$@CNTs cathodes (Figure S9, Supporting Information) have the relatively larger polarization (ΔE) of potentials and lower specific capacity at each current density. Figure S10 (Supporting Information) also presents the cycling performances of batteries with different cathodes evaluated at a current density of 0.5 C, in which V-MoS$_2$@CNT$_1$/S batteries show an excellent discharge specific capacity of 999.1 mAh g^{-1} after 150 cycles. In

© 2025 Wiley-VCH GmbH

Table 1. Comparison of electrochemical properties of Li-S batteries based on MoS_2 in recent works.

Active materials	Maximum capacity	Rate capacity	Fading rate [%]	
			Low rate	High rate
V-MoS$_2$@CNT$_1$/S (this work)	**1275/0.2 C**	**796/5 C**	**0.1/0.5 C**	**0.052/1 C**
$Zn_{0.12}MoS_2$-CNF/S[29]	1325/0.1 C	698/3 C	–	0.045/1 C
MoS_2/rGO-5.6[13]	1268/0.2 C	800/4 C	0.13/0.2 C	0.041/1 C
MoS_2-SnS/NC-PP[30]	1504/0.1 C	794/4 C	0.25/0.2 C	0.07/4 C
N-MoS_2 NHTs@S[16]	1146/0.2 C	632/4 C	0.07/0.2 C	0.044/1 C
Co_9S_8@MoS_2/CNF[31]	1221/0.1 C	477/5 C	0.09/0.1 C	0.091/1 C
Co-MoS_2-G/S[8]	1220/0.3 C	941/2 C	–	0.04/1 C
Pd/OMC[32]	1256/0.2 C	998/2 C	0.094/1 C	0.031/2 C
B/2D MOF-Co/PP[33]	1112/0.1 C	478/5 C	0.13/0.5 C	0.07/1 C
MoS_2/PP[34]	1471/0.1 C	550/1 C	0.08/0.5 C	–

comparison, the capacities of V-MoS_2@CNT_1/S, V-MoS_2@CNT_2/S and MoS_2@CNT_2/S are 870.4, 830.8, and 689.1 mAh g^{-1}, respectively. Meanwhile, V-MoS_2@ CNT_1/S cathodes have a good cycling stability with a coulombic efficiency close to 100%, which indicates that V-MoS_2@CNT_1 can greatly inhibit the shuttle effect of LiPSs and enhance the sulfur utilization. The long-term cycling stability of V-MoS_2@CNT_1/S, V-MoS_2@CNT_2/S, V-MoS_2@CNT_2/S, and MoS_2@CNT_1/S batteries at 1 C are further investigated. As shown in Figure 5h, V-MoS_2@CNT_1/S cathodes still show a high specific capacity of 692.3 mAh g^{-1} after 550 cycles and also carry out an outstanding capacity decay rate of 0.052% per cycle, which is superior to most of reported MoS_2-based Li-S batteries (**Table 1**). In contrast, the V-MoS_2@CNT_2/S (643.7 mAhg^{-1}), V-MoS_2@CNT_3/S (573.9 mAh g^{-1}) and MoS_2@CNT/S (441.2 mAh g^{-1}) cathodes show diminishing discharge capacity in cycles. Moreover, the electrochemical properties of MoS_2@CNT_1/S are shown in Figure S31 (Supporting Information). These results indicate that the uniform circumferential strain in MoS_2 layers with V dopants can accelerate the kinetics of the redox reaction of sulfur, reduce the shuttle effect of LiPSs, and contribute to the cycling stability. Additionally, high energy density is the key to the practical application of Li-S batteries, and the electrochemical performance of high sulfur-loaded Li-S batteries has been measured as shown in Figure 5i. The V-MoS_2@CNT_1/S cathodes are tested at a high sulfur loading of 3.8 mg cm^{-2}, while still show a high energy density of 3.2 mAh cm^{-2} at 20 µl of electrolyte (total amount) within 65 cycles at 0.1 C. In order to explore the practical use of curvature-dependent electrocatalytic activity in Li-S chemistry, V-MoS_2@CNT_2/PP is also used as the functionalized separator for Li-S batteries, and photographs of PP and V-MoS_2@CNT_2 modified separators are shown in Figure S11 (Supporting Information). Meanwhile, EIS tests (Figure S12, Supporting Information) performed with symmetric cells assembled using different separators showed that V-MoS_2 has a strong conversion capacity. Figure 5j shows the cycling performance of Li||Li symmetric batteries with V-MoS_2@CNT_2/PP separators in 1600 h cycles at a current density of 1 mA cm^{-2} and a stationary capacity of 1 mAh cm^{-2}, which also maintains a low and stable overpotential of 13 mV. Meanwhile, the symmetric battery with commercial PP separators exhibits high overpotential of 90 mV at only 800 h. Besides, the symmetric battery assembled with V-MoS_2@CNT_2/PP separators delivers satisfactory rate performance, which displays low overpotentials of 13.6, 16.4, 24.2, and 53.4 mV at current densities of 0.5, 1, 2, and 5 mA cm^{-2}, respectively (Figure S13, Supporting Information), and the overpotential maintains a value of 10.4 mV when the current density switches back to 0.5 mA cm^{-2}. To further explore the large-scale application of this circumferential strain effect on V-MoS_2@CNTs heterostructures, the capabilities of Li-S pouch cells with V-MoS_2@CNT_1/S cathodes are also teste, the internal structure and discharge capacity of the pouch cell is shown in Figure S14 (Supporting Information).

In order to straightforwardly reveal the circumferential strain effects on redox reaction kinetics of V-MoS_2@CNTs cathodes during charge/discharge process, in situ XRD tests are carried out with V-MoS_2@CNT_1/S and V-MoS_2@CNT_3/S cathodes. The schematic structure of the device for tests is shown in Figure S15 (Supporting Information). As shown in **Figure 6a–c**, the PXRD is shown in Figure S29 (Supporting Information), for V-MoS_2@CNT_1/S cathodes, the initial diffraction peaks observed at 23.03°, 26.73°, 27.77°, and 28.77° correspond to α-S_8 (JCPDS NO.77-0145). During the discharge process, the diffraction peaks of α-S_8 generally disappear at 1.99 V, indicating the complete conversion of α-S_8 to LiPSs. Besides, when the discharge potential arrives at 1.96 V, a new diffraction peak (26.8°) which belongs to Li_2S (111) crystalline surface appears and becomes even stronger until totally discharged. Oppositely, during the charge process, the peak intensity of Li_2S (111) generally diminishes. Then, the diffraction peak of β-S_8 (26°) gradually appears at 2.52 V, indicating the fast change of Li_2S to β-S_8. It should be indicated that the characteristic peaks of LiPSs are not clearly observed during charge/discharge process, which can be the results of their amorphous structures.[35] Thus, further detailed observation about the formation of intermediate products, e.g. Li_2S_8 and Li_2S_6, is provided in **Figure 7** by in situ Raman characterization. In contrast, for the in situ XRD results of V-MoS_2@CNT_3/S cathodes, there is no obvious Li_2S diffraction peaks which have been detected, which indicating the incomplete transformation process of S—LiPSs—Li_2S in V-MoS_2@CNT_3/S cathodes due to the less circumferential strain effect. In order to systematically quantify

16163028, 2025, 26, Downloaded from https://advanced.onlinelibrary.wiley.com/doi/10.1002/adfm.202422689 by WUHAN UNIVERSITY OF TECHNOLOGY, Wiley Online Library on [05/09/2025]. See the Terms and Conditions (https://onlinelibrary.wiley.com/terms-and-conditions) on Wiley Online Library for rules of use; OA articles are governed by the applicable Creative Commons License

16163028, 2025, 26, Downloaded from https://onlinelibrary.wiley.com/doi/10.1002/adfm.202422689 by WUHAN UNIVERSITY OF TECHNOLOGY, Wiley Online Library on [05/09/2025]. See the Terms and Conditions (https://onlinelibrary.wiley.com/terms-and-conditions) on Wiley Online Library for rules of use; OA articles are governed by the applicable Creative Commons License

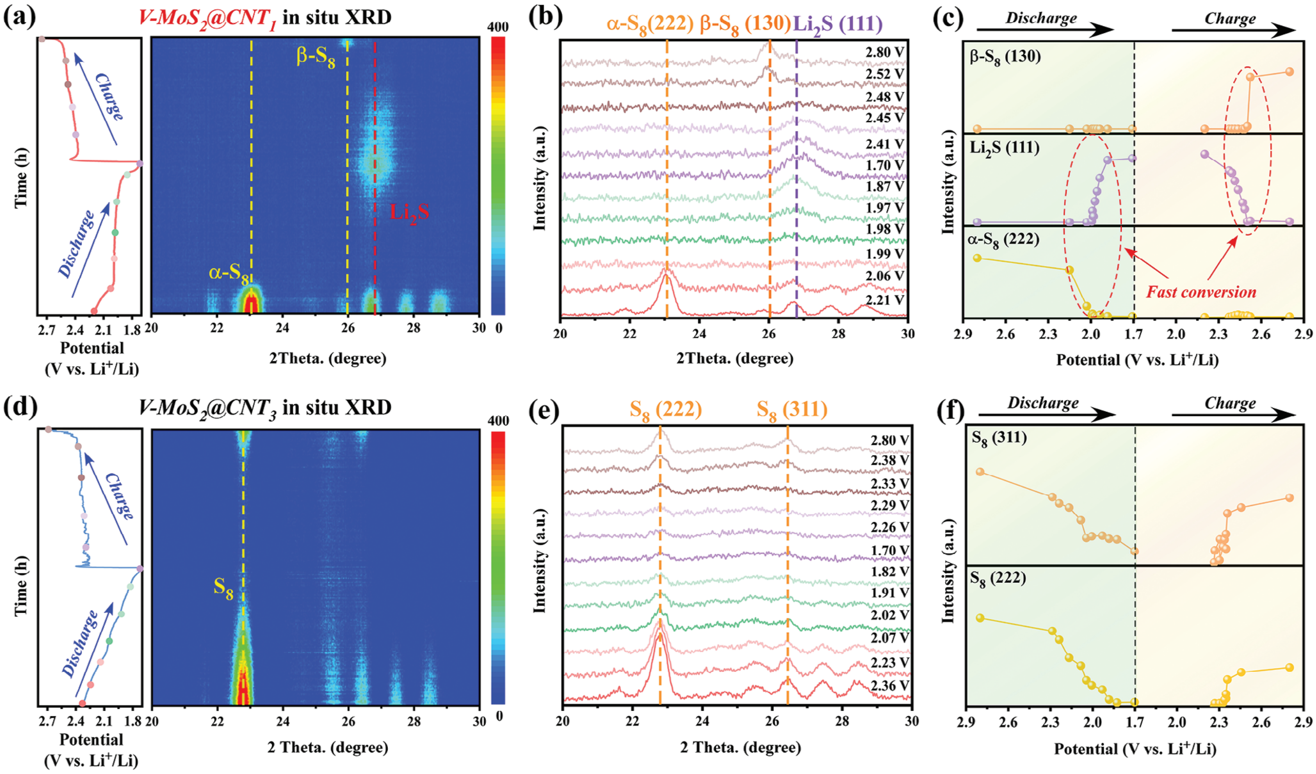

Figure 6. In situ XRD characterization of the curvature-dependent electrocatalytic kinetics in Li-S chemistry. a,d) GCD curves during the in situ XRD measurements (0.2 C) and corresponding contour plots of XRD patterns with V-MoS$_2$@CNT$_1$/S (a) and V-MoS$_2$@CNT$_3$/S (d) cathodes. b,e) In situ XRD patterns at different voltage states with V-MoS$_2$@CNT$_1$/S (b) and V-MoS$_2$@CNT$_3$/S (e) cathodes. g,h) Trend diagram of peak intensity changes of α-S$_8$ (222), Li$_2$S (111) and β-S$_8$ (130) with V-MoS$_2$@CNT$_1$/S cathodes (g) and that of S$_8$ (222) and S$_8$ (311) with V-MoS$_2$@CNT$_3$/S electrodes (h) as a function of potential.

the redox reaction of LiPSs in different cathodes, the peak intensity of α-S$_8$ (222), Li$_2$S (111), and β-S$_8$ (130) at different potentials during charge/discharge process is quantitatively plotted in Figure 6c,f. Compared with V-MoS$_2$@CNT$_3$ cathodes with less strain effect, V-MoS$_2$@CNT$_1$ cathodes always show a fast conversion kinetic within a short discharge/charge potential range. These time-resolved XRD results verifies that the circumferential strain effect on V-MoS$_2$@CNTs heterostructures can significantly improve the conversion reaction kinetics of LiPSs in Li-S chemistry, which is consistent with conclusions in previous electrochemical tests in Figure 4.

Furthermore, in situ Raman technique is also performed on V-MoS$_2$@CNT$_1$ and V-MoS$_2$@CNT$_3$ cathodes (details in Figure S16, Supporting Information). As shown in Figure 7a,d, two characteristic Raman bands of MoS$_2$ can be detected at 403 and 371 cm^{-1} and remain unchanged during charge/discharge process in both cathodes. Distinctively, for V-MoS$_2$@CNT$_1$, three peaks of S$_8$ (208.7, 461.8 and 141.5 cm^{-1}) sharply disappeared and the signal of S$_8{}^{2-}$ at 480.2 cm^{-1}, corresponding to long-chain Li$_2$S$_8$, appears at the initial stage during discharge. Then, the signal of S$_8{}^{2-}$ gradually convers to the signals of S$_6{}^{2-}$ (395.3 cm^{-1}), which is attributed to the formation of Li$_2$S$_6$.[36] When the discharge potential reaches at 2.15 V, the Raman signal of S$_6{}^{2-}$ becomes weakened, while the signal of S$_4{}^{2-}$ (373.7 cm^{-1}) appears.[28] On the contrary, for MoS$_2$@CNT$_3$ cathode, the conversion speed of LiPSs become much slowly by comparing the Raman signals of intermediate products in different cathodes at same potentials (Figure 7c,f). Overall, it can be concluded that the circumferential strain effect on V-MoS$_2$@CNTs heterostructures can accelerate the conversion of sulfur to each intermediate product (e.g., Li$_2$S$_8$, Li$_2$S$_6$, and Li$_2$S$_4$) and finally to insoluble Li$_2$S, resulting in the prevention of shuttling effect caused by LiPSs and well cycling stability of Li-S batteries.[24,37]

To further investigate the underlying correlation between the circumferential strain and the electrocatalytic activity in SRR of V-MoS$_2$@CNTs heterostructures, DFT calculations are provided to support the abovementioned experimental explanations. The models of MoS$_2$, V-MoS$_2$, curved MoS$_2$, and curved V-MoS$_2$ are shown in Figure S17 (Supporting Information). **Figure 8a** shows the charge density difference diagrams of *Li$_2$S$_4$ adsorption on MoS$_2$, V-MoS$_2$, curved MoS$_2$, and curved V-MoS$_2$. Relatively, the more notable charge redistributions after V doping and curved strain reveal the stronger interaction. Bader charge analysis also shows that curved V-MoS$_2$ (1.08 |e|) exhibits a larger amount of charge transfer from substrates to LiPSs compared to that in MoS$_2$ (0.24 |e|), V-MoS$_2$ (0.88 |e|) and curved MoS$_2$ (1.04 |e|), indicating the enhanced adsorption of LiPSs. For gaining deeper insights into the different adsorption behaviors of *Li$_2$S$_4$, the projected crystal orbital Hamilton population (pCOHP) between *Li$_2$S$_4$ group and the corresponding adsorption site on MoS$_2$, V-MoS$_2$, curved MoS$_2$ and curved V-MoS$_2$ was analyzed,

© 2025 Wiley-VCH GmbH

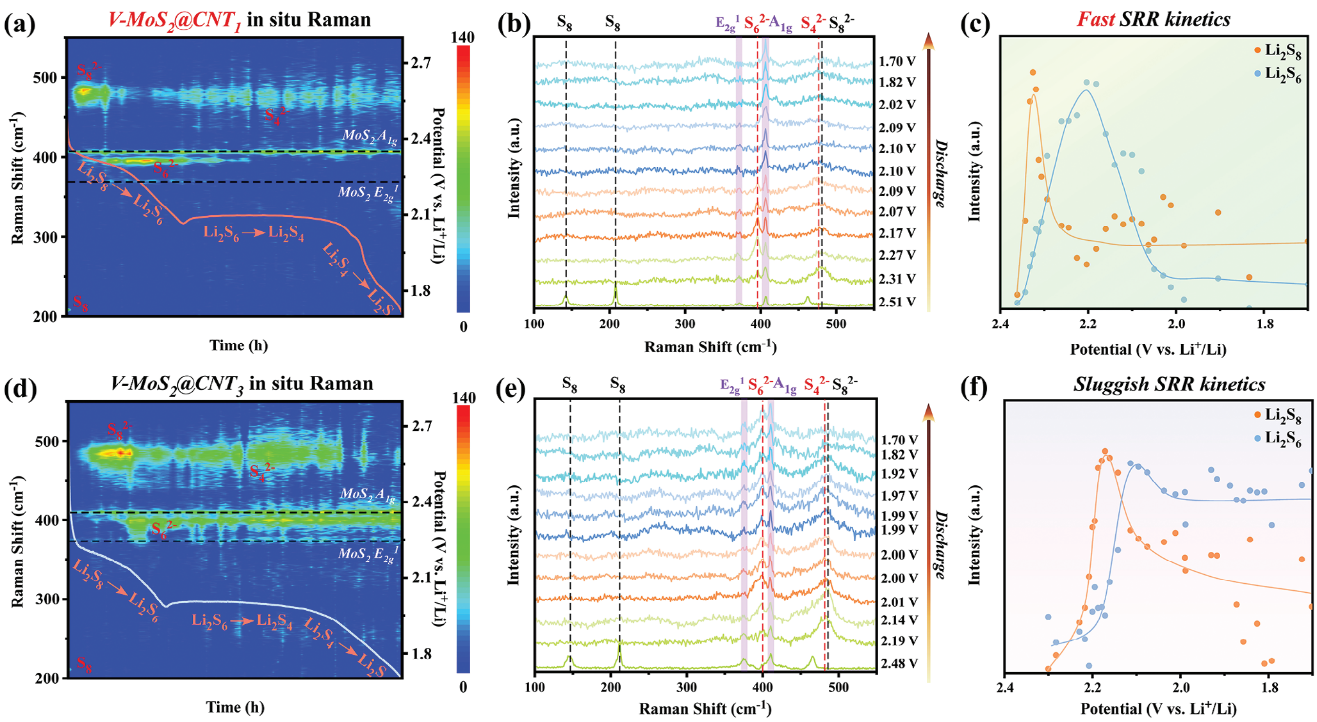

Figure 7. In situ Raman characterization of the curvature-dependent electrocatalytic kinetics in Li-S chemistry. a,d) GCD curves during in situ Raman test (at 0.2 C) and the corresponding contour plots of Raman spectra with V-MoS_2@CNT_1/S (a) and V-MoS_2@CNT_3/S (d) cathodes. b,e) Raman spectra extracted from (a) and (b) at different potentials with MoS_2@CNT_1/S (b) and V-MoS_2@CNT_3/S (e) cathodes. c,f) Trend diagram of peak intensity changes of Li_2S_8 and Li_2S_6 with V-MoS_2@CNT_1/S (c) and V-MoS_2@CNT_3/S (f) cathodes as a function of potentials, which can be used to determine the kinetics of SRR in different cathodes.

respectively (Figure 8b). It clearly shows that considerable bonding states are located below the Fermi level after introduction of V doping and curved strain, manifesting much more occupation and stronger $^*Li_2S_4$ bonding with V doping and curved strain MoS_2 than with pristine MoS_2. Furthermore, the integrated COHP (ICOHP) values were calculated to be −0.228, −0.308, and −0.318 eV in V-MoS_2, curved MoS_2, and curved V-MoS_2, which is more negative than the value of −0.195 eV in MoS_2, further suggesting the stronger $^*Li_2S_4$ adsorption after modification of V doping and curved strain. Moreover, the changes of electronic structure after introduction of V doping and curved strain were investigated. Figure 8c shows the calculated partial density of states (pDOS) of Mo and S atoms in MoS_2, V-MoS_2, curved MoS_2. After V doping or curved strain, an upward shift of pDOS with respect to the Fermi level for both of Mo and S atoms can be clearly found, signifying the promoted interaction between adsorbates and substrates, resulting in the stronger binding strength of $^*S_8$, $^*Li_2S_8$, $^*Li_2S_6$, $^*Li_2S_4$, $^*Li_2S_2$, and $^*Li_2S$ on curved V-MoS_2 with adsorption energies of −1.50, −2.30, −2.14, −2.93, −3.22, and −4.30 eV, respectively (Figure S18, Supporting Information). The optimized configurations for the binding of $^*S_8$, $^*Li_2S_8$, $^*Li_2S_6$, $^*Li_2S_4$, $^*Li_2S_2$, and $^*Li_2S$ to MoS_2, V-MoS_2, curved MoS_2 and curved V-MoS_2 are shown in Figures S19–S22 (Supporting Information).

In order to further understand the significantly promoted activity for reduction of LiPSs, the Gibbs free energy variation of elementary steps along the pathway of $^*S_8 \rightarrow {}^*Li_2S_8 \rightarrow {}^*Li_2S_6 \rightarrow {}^*Li_2S_4 \rightarrow {}^*Li_2S_2 \rightarrow {}^*Li_2S$ on MoS_2, V-MoS_2, curved MoS_2, and curved V-MoS_2 was investigated (Figure 8d). Clearly, it is noted that the formation of $^*Li_2S$ group in all cases is most endothermic step. Especially, the uphill energy of this step on curved V-MoS_2 is 0.99 eV, which is remarkably lower than that on MoS_2 (2.01 eV), V-MoS_2 (1.93 eV), and curved MoS_2 (1.18 eV), delivering an energetically smoother free energy profiles, responsible for effectively facilitating the reduction of LiPSs upon V doping and curved strain. Besides, it can be concluded that the circumferential strain effect plays a more critical role in reducing the energy barrier of rate limited step ($^*Li_2S_2$-$^*Li_2S$) when compared with the V-doping effect. In addition, the energy barrier profiles of $^*Li_2S$ decomposition into $^*LiS$ and $^*Li$ over MoS_2, V-MoS_2, curved MoS_2, and curved V-MoS_2 was presented in Figure 8e. The MoS_2 displays the highest $^*Li_2S$ decomposition barrier of 0.95 eV, while V-MoS_2 and curved MoS_2 shows slightly lower energy barriers of 0.65 and 0.55 eV, indicating the promoted catalytic reaction kinetic. Besides, upon the simultaneous introduction of V doping and curved strain, the $^*Li_2S$ decomposition barrier can be further reduced to 0.37 eV, signifying the accelerated $^*Li_2S$ decomposition and rapid oxidation of $^*Li_2S$ during charging, thereby enhancing the redox reversibility of Li-S chemistry, which is consistent with the galvanostatic charge-discharge profiles. Overall, these results confirm that the customization of V doping and curved strain can achieve the simultaneous improvement of adsorption capabilities and catalytic reaction dynamics and facilitate the conversion of LiPSs, ultimately enhancing the electrochemical performance of Li-S batteries.

© 2025 Wiley-VCH GmbH

16163028, 2025, 26, Downloaded from https://advanced.onlinelibrary.wiley.com/doi/10.1002/adfm.202422689 by WUHAN UNIVERSITY OF TECHNOLOGY, Wiley Online Library on [05/09/2025]. See the Terms and Conditions (https://onlinelibrary.wiley.com/terms-and-conditions) on Wiley Online Library for rules of use; OA articles are governed by the applicable Creative Commons License

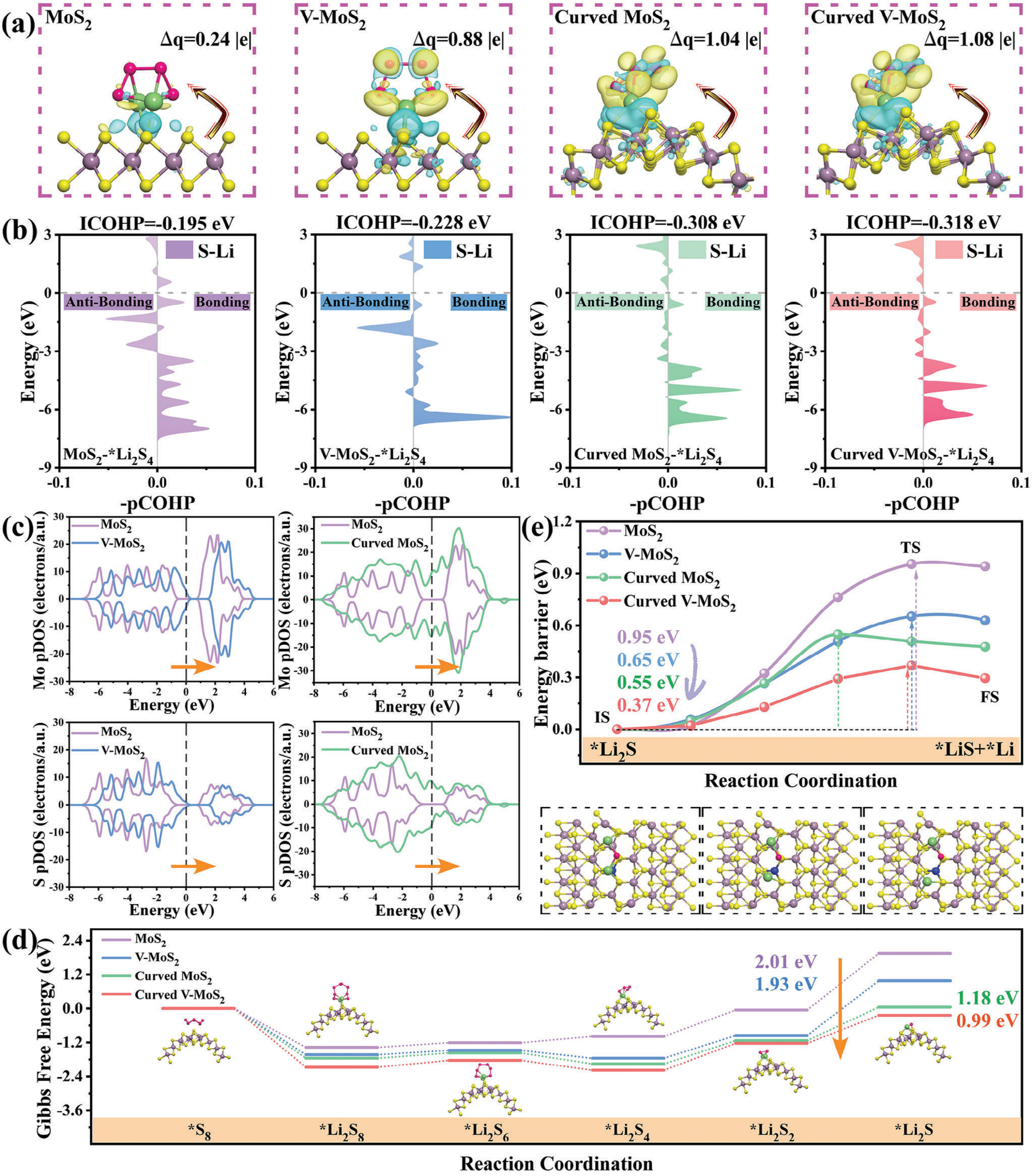

Figure 8. Theoretical investigation of circumferential strain effect and V doping on the reduction of LiPSs. a) Optimized $^*Li_2S_4$ adsorption models of MoS_2, V-MoS_2, curved MoS_2 and curved V-MoS_2, along with the Bader charge analyses and charge density differences (isosurface value 1.5×10^{-3} |e|/bohr^3) between $^*Li_2S_4$ group and corresponding substrates, in which yellow and cyan represent charge accumulation and depletion, respectively (Purple: Mo atoms; yellow: S atoms in substrates; red: S atoms in LiPSs; green: Li atoms; blue: V atoms). b) pCOHP and ICOHP analyses between $^*Li_2S_4$ group and their corresponding adsorption sites over MoS_2, V-MoS_2, curved MoS_2 and curved V-MoS_2. c) Calculated pDOS of Mo and S atoms with and without V doping and curved strain. d) Gibbs free energy profiles for the reduction of LiPSs on MoS_2, V-MoS_2, curved MoS_2 and curved V-MoS_2. e) Energy barrier profiles of the $^*Li_2S$ decomposition on MoS_2, V-MoS_2, curved MoS_2 and curved V-MoS_2. The structures of each state along the reaction path on curved V-MoS_2 are shown by insets, while the other can be found in Figures S23–S25 (Supporting Information).

© 2025 Wiley-VCH GmbH

16163028, 2025, 26, Downloaded from https://advanced.onlinelibrary.wiley.com/doi/10.1002/adfm.202422689 by WUHAN UNIVERSITY OF TECHNOLOGY, Wiley Online Library on [05/09/2025]. See the Terms and Conditions (https://onlinelibrary.wiley.com/terms-and-conditions) on Wiley Online Library for rules of use; OA articles are governed by the applicable Creative Commons License

3. Conclusion

In summary, this work introduces a feasible way to the scale-up synthesis of high-performance SACs with tunable curvature-dependent electrocatalytic activities. Benefited from the time-resolved characterizations, the underlying regulating mechanism revealed in this work, which is caused by uniform circumferential strain in V-MoS_2@CNTs heterostructures, deepens the understanding of strain engineering in SRR. V-MoS_2@CNTs heterostructures with the strongest circumferential strain exhibit a sparkle discharge capacity of 1202 mAh g^{-1} at 0.5 C and a capacity fading of 0.052% at 1 C, while an outstanding rate performance of 796 mAh g^{-1} at 5 C. In addition, the considerable behavior of V-MoS_2@CNTs cathodes with a high sulfur loading and further applications in the modified separators of Li-S batteries also shows the potential industrial value of this work. The unique synthetic strategy and regulatory mechanism of circumferential strain confirmed here pave a special way for the design of high-performance electrocatalysts in energy storage and conversion devices beyond Li-S batteries, e.g. metal-air batteries, redox flow batteries, and fuel cells.

Supporting Information

Supporting Information is available from the Wiley Online Library or from the author.

Acknowledgements

K.W. and Y.W. contributed equally to this work. This work was financially supported by the National Natural Science Foundation of China (No. 62474127, 52127816), the National Key Research and Development Program of China (2023YFB3809301) and the Chongqing Natural Science Foundation (CSTB2024NSCQ-MSX0991). Authors greatly thank Prof. Liqiang Mai in Wuhan University of Technology for his carefully discussion and financial support on this work. Besides, authors would like to appreciate the SLRI Synchrotron Radiation Optical Institute (Public Organization) for the beam time provided, and this work was supported by Dr. Suttipong Wannapaiboon and the beamline 1.1W staffs.

Conflict of Interest

The authors declare no conflict of interest.

Data Availability Statement

The data that support the findings of this study are available in the supplementary material of this article.

Keywords

circumferential strain engineering, heterostructures, Li-S chemistry, single-atom catalysts, sulfur redox reaction

Received: November 20, 2024
Revised: January 8, 2025
Published online: February 3, 2025

[1] a) Z. W. Seh, Y. Sun, Q. Zhang, Y. Cui, *Chem. Soc. Rev.* **2016**, *45*, 5605; b) P. G. Bruce, S. A. Freunberger, L. J. Hardwick, J.-M. Tarascon, *Nat. Mater.* **2011**, *11*, 19; c) X. Ji, K. T. Lee, L. F. Nazar, *Nat. Mater.* **2009**, *8*, 500; d) C. Zhou, C. Dong, W. Wang, Y. Tian, C. Shen, K. Yan, L. Mai, X. Xu, *Interdiscip. Mater.* **2024**, *3*, 306.
[2] a) H. Pan, J. Chen, R. Cao, V. Murugesan, N. N. Rajput, K. S. Han, K. Persson, L. Estevez, M. H. Engelhard, J.-G. Zhang, K. T. Mueller, Y. Cui, Y. Shao, J. Liu, *Nat. Energy* **2017**, *2*, 813; b) Q. Wu, Z. Yao, X. Zhou, J. Xu, F. Cao, C. Li, *ACS Nano* **2020**, *14*, 3365; c) Z. Ye, Y. Jiang, L. Li, F. Wu, R. Chen, *Adv. Mater.* **2020**, *32*, 2002168; d) A. Bhargav, J. He, A. Gupta, A. Manthiram, *Joule* **2020**, *4*, 285; e) L. Luo, S. H. Chung, H. Yaghoobnejad Asl, A. Manthiram, *Adv. Mater.* **2018**, *30*, 1804149; f) F. Pei, L. Lin, A. Fu, S. Mo, D. Ou, X. Fang, N. Zheng, *Joule* **2018**, *2*, 323.
[3] a) A. Manthiram, S. H. Chung, C. Zu, *Adv. Mater.* **2015**, *27*, 1980; b) H. Xu, Q. Jiang, K. S. Hui, S. Wang, L. Liu, T. Chen, Y. Zheng, W. F. Ip, D. A. Dinh, C. Zha, Z. Lin, K. N. Hui, *ACS Nano* **2024**, *18*, 8839.
[4] a) S. D. Seo, D. Park, S. Park, D. W. Kim, *Adv. Funct. Mater.* **2019**, *29*, 1903712; b) Z. Cheng, Z. Xiao, H. Pan, S. Wang, R. Wang, *Adv. Energy Mater.* **2017**, *8*, 1702337; c) P. Chen, T. Wang, F. Tang, G. Chen, C. Wang, *Chem. Eng. J.* **2022**, *446*, 136990; d) C. Huang, J. Yu, C. Y. Zhang, Z. Cui, J. Chen, W. H. Lai, Y. J. Lei, B. Nan, X. Lu, R. He, L. Gong, J. Li, C. Li, X. Qi, Q. Xue, J. Y. Zhou, X. Qi, L. Balcells, J. Arbiol, A. Cabot, *Adv. Mater.* **2024**, *36*, 2400810.
[5] Y. Cao, Y. Lin, J. Wu, X. Huang, Z. Pei, J. Zhou, G. Wang, *ChemSusChem* **2019**, *13*, 1392.
[6] Z. Cheng, Y. Chen, Y. Yang, L. Zhang, H. Pan, X. Fan, S. Xiang, Z. Zhang, *Adv. Energy Mater.* **2021**, *11*, 2003718.
[7] Y. Tian, G. Li, Y. Zhang, D. Luo, X. Wang, Y. Zhao, H. Liu, P. Ji, X. Du, J. Li, Z. Chen, *Adv. Mater.* **2019**, *32*, 1904876.
[8] W. Liu, C. Luo, S. Zhang, B. Zhang, J. Ma, X. Wang, W. Liu, Z. Li, Q.-H. Yang, W. Lv, *ACS Nano* **2021**, *15*, 7491.
[9] Z. Ma, Y. Liu, J. Gautam, W. Liu, A. N. Chishti, J. Gu, G. Yang, Z. Wu, J. Xie, M. Chen, L. Ni, G. Diao, *Small* **2021**, *17*, 2102710.
[10] a) Z. Liang, J. Shen, X. Xu, F. Li, J. Liu, B. Yuan, Y. Yu, M. Zhu, *Adv. Mater.* **2022**, *34*, 2200102; b) G. Dai, S. Li, M. Shi, L. Sun, Y. Jiang, K. N. Hui, Z. Ye, *Adv. Funct. Mater.* **2024**, *34*, 2315563.
[11] W. Wang, X. Wang, J. Shan, L. Yue, Z. Shao, L. Chen, D. Lu, Y. Li, *Energy Environ. Sci.* **2023**, *16*, 2669.
[12] a) J. Su, C. B. Musgrave, Y. Song, L. Huang, Y. Liu, G. Li, Y. Xin, P. Xiong, M. M.-J. Li, H. Wu, M. Zhu, H. M. Chen, J. Zhang, H. Shen, B. Z. Tang, M. Robert, W. A. Goddard, R. Ye, *Nat. Catal.* **2023**, *6*, 818; b) T. Zhang, Q. Ye, Z. Han, Q. Liu, Y. Liu, D. Wu, H. J. Fan, *Nat. Commun.* **2024**, *15*, 6508.
[13] C. Zhao, Y. Huang, B. Jiang, Z. Chen, X. Yu, X. Sun, H. Zhou, Y. Zhang, N. Zhang, *Adv. Energy Mater.* **2023**, *14*, 2302586.
[14] C. Y. Zhang, C. Zhang, J. L. Pan, G. W. Sun, Z. Shi, C. Li, X. Chang, G. Z. Sun, J. Y. Zhou, A. Cabot, *eScience* **2022**, *2*, 405.
[15] X. Zhang, F. Zhou, S. Zhang, Y. Liang, R. Wang, *Adv. Sci.* **2019**, *6*, 1900090.
[16] W. Shen, P. Li, Q. Zhang, E. Han, G. Gu, R. Wang, X. Li, *Small* **2023**, *19*, 2304122.
[17] M. Suleman, S. Lee, M. Kim, M. Riaz, Z. Abbas, H.-m. Park, V. H. Nguyen, N. Nasir, S. Kumar, J. Jung, Y. Seo, *Mater. Today Phys.* **2024**, *43*, 101427.
[18] X. Xu, T. Liang, D. Kong, B. Wang, L. Zhi, *Mater. Today Nano* **2021**, *14*, 100111.
[19] a) L. Yang, Y. Pan, Z. Zhou, Y. Zhang, J. Xu, C. Ma, Y. Zhang, J. Wang, W. Qiao, L. Ling, *ACS Nano* **2023**, *17*, 17405; b) H. Cheng, Z. Shen, W. Liu, M. Luo, F. Huo, J. Hui, Q. Zhu, H. Zhang, *ACS Nano* **2023**, *17*, 14695; c) Y. Zhang, C. Ma, C. Zhang, L. Ma, S. Zhang, Q. Huang, C. Liang, L. Chen, L. Zhou, W. Wei, *Chem. Eng. J.* **2023**, *452*, 139410.
[20] X. Du, J. Huang, J. Zhang, Y. Yan, C. Wu, Y. Hu, C. Yan, T. Lei, W. Chen, C. Fan, J. Xiong, *Angew. Chem., Int. Ed.* **2019**, *58*, 4484.

16163028, 2025, 26, Downloaded from https://advanced.onlinelibrary.wiley.com/doi/10.1002/adfm.202422689 by WUHAN UNIVERSITY OF TECHNOLOGY, Wiley Online Library on [05/09/2025]. See the Terms and Conditions (https://onlinelibrary.wiley.com/terms-and-conditions) on Wiley Online Library for rules of use; OA articles are governed by the applicable Creative Commons License

[21] a) J. Ge, D. Zhang, Y. Qin, T. Dou, M. Jiang, F. Zhang, X. Lei, *Appl. Catal., B* **2021**, *298*, 120557; b) B. Ravel, M. Newville, *J. Synchrotron Radiat.* **2005**, *12*, 537.

[22] C. Dong, C. Zhou, M. Wu, Y. Yu, K. Yu, K. Yan, C. Shen, J. Gu, M. Yan, C. Sun, L. Mai, X. Xu, *Adv. Energy Mater.* **2023**, *13*, 2301505.

[23] C. Wang, R. Liu, W. Liu, W. Zhu, X. Yang, Q. Wu, K. Xie, L. Shen, J. Wu, Y. Liu, L. He, Z. Chen, J. Chen, C. Zhao, X. Lin, L. Shi, J. Zhao, X. Feng, G. Wu, Y. Ma, *Adv. Funct. Mater.* **2024**, *34*, 2316221.

[24] X. Li, Y. Zuo, Y. Zhang, J. Wang, Y. Wang, H. Yu, L. Zhan, L. Ling, Z. Du, S. Yang, *Adv. Energy Mater.* **2024**, *14*, 2303389.

[25] H. Xu, Q. Jiang, Z. Shu, K. S. Hui, S. Wang, Y. Zheng, X. Liu, H. Xie, W. F. Ip, C. Zha, Y. Cai, K. N. Hui, *Adv. Sci.* **2024**, *11*, 2307995.

[26] G. Liu, Q. Zeng, X. Sui, S. Tian, X. Sun, Q. Wu, X. Li, Y. Zhang, K. Tao, E. Xie, Z. Zhang, *Small* **2023**, *19*, 2301085.

[27] H. Li, W. Zheng, H. Wu, Y. Fang, L. Li, W. Yuan, *Small* **2023**, *20*, 2306140.

[28] X. Wu, R. Xie, D. Cai, B. Fei, C. Zhang, Q. Chen, B. Sa, H. Zhan, *Adv. Funct. Mater.* **2024**, *34*, 2315012.

[29] M. Jin, G. Sun, Y. Wang, J. Yuan, H. Zhao, G. Wang, J. Zhou, E. Xie, X. Pan, *ACS Nano* **2024**, *18*, 2017.

[30] J. Zhang, W. Xi, F. Yu, Y. Zhang, R. Wang, Y. Gong, B. He, H. Wang, J. Jin, *Chem. Eng. J.* **2023**, *475*, 146009.

[31] B. Li, Q. Su, L. Yu, J. Zhang, G. Du, D. Wang, D. Han, M. Zhang, S. Ding, B. Xu, *ACS Nano* **2020**, *14*, 17285.

[32] Y. Sun, J. Wang, T. Shang, Z. Li, K. Li, X. Wang, H. Luo, W. Lv, L. Jiang, Y. Wan, *Angew. Chem., Int. Ed.* **2023**, *62*, 202306791.

[33] Y. Li, S. Lin, D. Wang, T. Gao, J. Song, P. Zhou, Z. Xu, Z. Yang, N. Xiao, S. Guo, *Adv. Mater.* **2020**, *32*, 1906722.

[34] Z. A. Ghazi, X. He, A. M. Khattak, N. A. Khan, B. Liang, A. Iqbal, J. Wang, H. Sin, L. Li, Z. Tang, *Adv. Mater.* **2017**, *29*, 1606817.

[35] Y. Luo, Z. Fang, S. Duan, H. Wu, H. Liu, Y. Zhao, K. Wang, Q. Li, S. Fan, Z. Zheng, W. Duan, Y. Zhang, J. Wang, *Angew. Chem., Int. Ed.* **2023**, *62*, 202215802.

[36] R. Liu, Z. Wei, L. Peng, L. Zhang, A. Zohar, R. Schoeppner, P. Wang, C. Wan, D. Zhu, H. Liu, Z. Wang, S. H. Tolbert, B. Dunn, Y. Huang, P. Sautet, X. Duan, *Nature* **2024**, *626*, 98.

[37] D. Yang, C. Li, M. Sharma, M. Li, J. Wang, J. Wei, K. Liu, Y. Zhang, J. Li, G. Henkelman, Q. Zhang, A. Cabot, *Energy Storage Mater.* **2024**, *66*, 103240.

© 2025 Wiley-VCH GmbH

16163028, 2025, 26, Downloaded from https://advanced.onlinelibrary.wiley.com/doi/10.1002/adfm.202422689 by WUHAN UNIVERSITY OF TECHNOLOGY, Wiley Online Library on [05/09/2025]. See the Terms and Conditions (https://onlinelibrary.wiley.com/terms-and-conditions) on Wiley Online Library for rules of use; OA articles are governed by the applicable Creative Commons License